Supporting Information Appendix

The WRF-Chem Model

To assess the impacts of biomass burning (BB) aerosols on the marine stratocumulus clouds, the WRF-Chem model version 3.6.1 (*1*) is configured with a domain covering both southern Africa and the southeast Atlantic as shown in Figure S9. The domain has a size of 6000 km (east-west) by 1800 km (south-north) with a horizontal resolution of 3 km, and 42 vertical layers (17 layers in the bottom 1 km). We conduct a series of 3-day forecasts by simulating the chemistry continuously from August 1 to September 30, 2014 but reinitializing time dependent meteorological initial and boundary conditions and sea surface temperatures with the NCEP FNL reanalysis data every two days. The chemistry fields by the end of day 2 are used in initializing the next 3-day simulation. 3-hourly model outputs from the last two days of the series forecasts are concatenated and analyzed.

An hourly BB aerosol emission dataset with 3 km spatial resolution is generated from the fire radiative power (FRP) technique (*2*). In this technique, the BB aerosol emission rate of each active fire is proportional to the FRP value retrieved by SEVIRI onboard the Meteosat satellite. The ratios, so-called emission coefficients, equal 18 g/MJ for savanna and grassland regions, and 15 g/MJ for tropical forest regions in southern Africa (*2*). A portion of East Africa is not included in the domain to save the computational costs, as the biomass burning emissions in this region only account for a very small fraction of total emissions (3.27%) during August and September of 2014. A plume rise model is coupled in the WRF-Chem model to calculate the injection height of BB aerosols. The plume rise model is driven by fire size, fire heat flux, and the ambient thermodynamic conditions (*3*).

When incorporated with the MOSAIC aerosol scheme in WRF-Chem, the BB aerosol emissions are further partitioned into black carbon (BC), organic matter (OM), and other inorganic components following the vegetation-dependent mass ratios defined in the Fire Inventory from NCAR (FINN) dataset (*4, 5*). Sea-salt and DMS emissions as well as chemical boundary layer conditions are treated as in (*6*). It should be noted that BB aerosols and dust particles that enter domain from north are not considered in this study, because, very likely their contributions to aerosol fields in the Southern Africa and SEA relatively are small.

The MOSAIC aerosol scheme in WRF-Chem uses a sectional approach with eight size bins to represent the aerosol size distribution. Different aerosol species within each size bin are assumed to be internally mixed so that all particles within a size bin have the same chemical composition. Aerosol optical properties are computed as a function of wavelength and three-dimensional position, and further coupled with the Goddard SW and RRTM LW schemes for the calculation of the radiative effect of BB aerosols. To simulate the aerosol microphysical effect, MOSAIC is coupled with the Abdul-Razzak and Ghan CCN activation parameterization (*7*), which is further coupled with the Morrison two-moment microphysics scheme (*6*). The other physics packages employed in this study include the Grell cumulus parameterization (designed for resolution finer than 3 km), Noah land surface model, and MYJ planetary boundary layer (PBL) scheme are used.

In order to elucidate the effects of BB aerosols on the diurnal cycle of stratocumulus, we simulated three cases. In C-case, only sea salt aerosol and DMS emissions are considered, while in P-case, the BB aerosol emissions are also incorporated. In M-case, we turned off the radiative effect of aerosols (dominantly due to BB aerosols by more than 90% in the fire seasons), so that the microphysical and semi-direct effects can be distinguished.

The WRF model in LES mode

In previous studies, LES substantially furthers our understanding of the processes/feedbacks regulating stratocumulus (*8-12*). As shown in Figure S9, we conduct four one-way nesting simulations using the WRF model (without chemistry package) over different regions over SEA. Unlike idealized large-eddy simulations, these nesting simulations are driven by the initial and boundary conditions generated from the meteorological fields modeled by WRF-Chem (P-case) using ndown.exe program (*13*). Simulations are run with two additional levels of nesting from 00UTC September 7 to 00UTC September 9. Each domain and its two inner nests cover areas of 600 km×600 km, 100 km×100 km, and 33.3 km×33.3 km with horizontal resolutions of 600 m, 200 m, and 66.7 m, respectively. In this study, we only analyze the cloud properties in the innermost nest since its horizontal resolution reaches the LES regime. The vertical resolution is further refined from 42 layers in WRF-Chem to 97 layers (with 52 layers within 0 to 1 km and 25 layers within 1 to 2 km). The model results are outputted every hour. The physics packages used are generally consistent with the ones used in the outer domain, except the chemistry package and cumulus parameterization are both turned off, and MYJ PBL scheme is replaced by LES PBL scheme with the Smagorinsky subgrid-scale (SGS) turbulence model (*14*).

For each one-way nesting simulation by WRF-LES, we designed a P-case and a C-case similar to those in the WRF-Chem, except the radiative and microphysical properties of BB aerosols are prescribed and horizontally uniform in the domain. To represent the radiative effect of BB aerosols in the model, we incorporated the vertical profiles of radiative properties of BB aerosols at four wavelengths (300, 400, 600, and 999 nm) modeled by WRF-Chem over the same area into the Goddard SW scheme. The profiles are shown in Figure S10.

To account for the microphysical effect of BB aerosols in WRF-LES, we employ N_d values for both P-case and C-case. N_d in C-case is set to 30 cm^{-3}, while a diurnal cycle of N_d is applied to P-case. N_d in P-case is updated every 3 hours (N_d = 100 cm^{-3} from 00 UTC to 09 UTC; 75 cm^{-3} from 09 UTC to 12 UTC; 50 cm^{-3} from 12 UTC to 18 UTC; 100 cm^{-3} from 18 UTC to 00 UTC). Even though the diurnal cycle of N_d averaged over study domain and period is not large (i.e. Figure 2A), we do apply the diurnal cycle of N_d in P-case because we find a 25 cm^{-3} reduction in N_d from morning to afternoon over the WRF-LES domains considered in our study as shown in MODIS retrievals (i.e. Figure S2).

Satellite observations in comparison with model simulations

To validate modeled aerosol, cloud, and radiation fields, we employ products from several sensors onboard different satellites, including MODIS, CALIOP, CATS, SEVIRI, and CERES.

Above-cloud AOD

As mentioned in the text above, the observed above-cloud AOD is derived from the reflectance measurements at six MODIS channels from the visible to the shortwave infrared (*15*). In this study, MODIS retrievals of above-cloud AODs are an aggregated level-3 product with 1° × 1° resolution. The values are weighted by aerosol pixel counts in each 1 by 1 degree. The WRF-Chem model does not directly output above-cloud AOD, but vertical profiles of layer AOD. Therefore, we first identify the cloud-top layer using a threshold cloud water mixing ratio (0.01 g kg^{-1}). Then by adding up layer AOD above the cloud-top layer, we obtain modeled above-cloud AOD.

In Figure S1 (A) and (B), we compare the above-cloud aerosol optical depth (AOD) fields from MODIS/Aqua retrievals and the P-case simulation over the SEA during the study period (from August to September 2014). We label the BB aerosol emissions in Figure S1 (A) and (B) by orange dots representing the total two-month emissions over an area of 150 km × 150 km. During the entire study period, 2.4 Tg of BB aerosols are emitted within the domain.

Cloud fraction (CF) and cloud liquid water path (LWP)

The modeled CF and LWP fields are compared against daily level-3 Terra and Aqua MODIS cloud products ("Cloud Retrieval Fraction Liquid" and "Cloud Water Path Liquid Mean") averaged over the study period. In order to calculate the MODIS LWP field averaged over the study period, the daily MODIS LWP is weighted by cloud pixel counts. Similar to (*6*), the modeled CF of each model column is assigned as 1 if cloud water mixing ratio is larger than 0.01 g kg^{-1} anywhere in a model column below 700 hPa; otherwise as 0. Because cloud properties are outputted every three hours, we average the cloud properties of two time steps in order to enable the comparison (e.g., the average value of model outputs at 9 UTC and 12 UTC is compared against Terra observation at 10:30 LST).

Figure S2 shows the modeled and observed CF and LWP fields during morning and afternoon averaged over the study period. The differences between model and observation in domain-averaged CF and LWP are less than 1.5% and 3 g m^{-2}, respectively. By examining CF and LWP fields, we find that the spatial distributions of CF are fairly well simulated. In addition, WRF-Chem successfully captures the breakup of stratocumulus clouds over the remote region far away from the coast during the daytime. The spatial distribution of LWP is reasonably simulated; however, WRF-Chem overestimates LWP by about 20 g m^{-2} over the region north of 5°S and underestimates LWP by about 20 g m^{-2} over the lower left corner of modeling domain (10°S to 18°S, 0° to 17°W). The bias in modeled LWP is mainly caused by the stratocumulus clouds that are intermittently coupled with the MBL or those with cumulus clouds embedded below. In addition to CF and LWP fields, WRF-Chem model is also capable of capturing meso-scale structures within the stratocumulus clouds, such as open cells (e.g., September 2), closed cells with high LWP values (e.g., September 5), and gravity wave breaking cloud decks (e.g., September 7), when compared to level-2 MODIS cloud water path product as shown in Figure S11.

To validate modeled CF, instead of the MODIS product "Cloud Fraction", we use "Cloud Retrieval Fraction Liquid" product. The former product tends to overestimate CF of stratocumulus because it includes ice cloud pixels (see an example case shown in Figure S12). The latter product probably underestimates CF because this product is calculated by counting MODIS level-2 pixels with successful COT and effective radius retrievals only; therefore, WRF-Chem likely underestimates the CF. In addition, the MODIS LWP retrievals are likely biased low due to low-biased cloud optical thickness retrievals as a result of above-cloud aerosol absorption at the 860 nm channel. The uncertainties associated with LWP (due to systematic errors in detecting and retrieval processes), as in Table S1, are obtained from level-3 MODIS cloud products, and averaged over the study period and domain.

Cloud droplet number concentration

In Figure S2, we compare N_d retrieved from MODIS observations against cloud-top N_d modeled by P-case averaged over the study period. Following the approach in (*16*), we calculate N_d from Terra and Aqua/MODIS level-3 cloud-top effective radius (r_e) and cloud optical depth (τ_c) products with assumptions ($N_d = K\tau_c^{1/2} r_e^{-5/2}$), where K equals to 1.125×10^{-6} $cm^{-1/2}$. The liquid water content at the top of the cloud is assumed to be 80% of the adiabatic value. The ratio between volume mean radius and the effective radius k equals 0.8 approximately. The values are further weighted by cloud pixel count. Compared to Terra and Aqua observations, modeled mean N_d values are slightly underestimated and overestimated, respectively, as in Table S1 (model vs. Terra: 90.6 cm^{-3} vs. 92.5 cm^{-3}; model vs. Aqua: 91.5 cm^{-3} vs. 85.3 cm^{-3}). In addition, the spatial pattern of N_d is reasonably simulated. Observed N_d can be biased due to biased r_e and τ_c. The level-3 MODIS cloud products report the uncertainties associated with cloud optical depth and cloud effective radius. Using possible ranges of cloud optical depth and the effect radius, we derived the range of N_d to be 63.9-128.6 cm^{-3} for Terra and 59.3-132.9 cm^{-3} for Aqua (Table S1).

Cloud optical depth (τ_c)

In Figure 2C, we compare modeled τ_c against level-3 MODIS cloud products ("Cloud Optical Depth Mean Liquid") averaged over the study domain and period. To be consistent with N_d calculation discussed above, we adopt the expression in Eq.6 of (*16*) for modeled $\tau_c = CN_d^{1/3}LWP^{5/6}$, where $C=0.2303\ m^{8/3}kg^{-5/6}$ is effectively a constant. As shown in Figure 2C, model performs reasonably well in simulating τ_c in terms of domain averaged values.

Vertical distributions of aerosols and cloud-top heights

In Figure S1 (C) and (D), we compare vertical profiles of relative occurrence frequencies of aerosol features and cloud-top heights in the coastal and remote regions. The values are obtained from CALIOP aerosol and cloud profile products with a horizontal resolution of 5 km (CAL_LID_L2_05kmAPro and CAL_LID_L2_05kmCPro). To calculate the vertical distribution of aerosols from CALIOP, we follow the approach in (*17*); however, instead of vertical feature mask product (VFM), we count non-zero values in "Extinction Coefficient 532" dataset. To calculate the vertical profiles of aerosol features from CATS observations, we count the pixels that are labeled as aerosols. Modeled vertical profiles of aerosol features are calculated similarly by counting model grids with extinction at wavelength 550 nm larger than a threshold value (0.05 km^{-1}). As shown in (*18*), the detection threshold of CALIOP for BB aerosols lies within about 0.01~0.1 km^{-1}; therefore, we select 0.05 km^{-1} as the threshold for modeled extinction.

To calculate both observed and modeled relative occurrence frequency of aerosol features, we consider cloud-free portions of the cloudy lidar profiles and model columns with stratocumulus clouds, count the aerosol features, and add the counts at a given level over both coastal and remote regions. We normalize the profiles by the total count of aerosol features between 0 to 6 km so that the areas between curve and Y-axis equal to one. We only analyze aerosol profiles during the nighttime because weakly scattering layers can be better detected than daytime (*19*); To calculate observed cloud-top heights, for each CALIOP profile, we examine the "Cloud Layer Fraction" product and identify cloud tops (below 700 hPa).

As shown in Figures S1 (C) and (D), WRF-Chem reasonably captures the transition of vertical distributions of aerosol features from the coastal to remote regions, except the model slightly overestimates the occurrence frequency of BB aerosols below 3 km near the coast, and produces a peak frequency at a lower altitude for the remote region. Figure S1 (C) and (D) also show the relative occurrence frequencies of cloud-top heights over the SEA as (C) observed by CALIOP (grey shaded area) and (D) modeled by the P-case (red bars) and C-case (blue bars) during the daytime of the study period. The model simulations, in agreement with the CALIOP observation, predict that the cloud-tops of stratocumuli increase as the MBL deepens from the coastal to remote regions.

Above-cloud aerosols (ACA) occurrence frequency

To calculate the modeled above-cloud aerosol (ACA) occurrence frequency, which is critical for estimating the DRE of BB aerosols (*20*), we count the numbers of model columns with low-level stratocumulus cloud and model columns with both low-level stratocumulus cloud and above-cloud AOD larger than 0.1. The ratio between two values is defined as occurrence frequency of ACA. According to Figure 6 in (*21*), the occurrence frequency of above-cloud AODs retrieved by MODIS below 0.1 is very low. Therefore, we use the threshold above-cloud AOD of 0.1 for ACA calculations.

Observed occurrence frequencies are obtained from two satellite products: 1) In CALIOP observations, we counted VFM along the swaths for August and September of 2014 (*20*). The differences in ACA occurrence frequencies obtained from daytime and nighttime observations are quite significant, because of different signal-to-noise ratios. In this study, we only compare modeled and observed nighttime ACA occurrence frequency; 2) Similarly, we also counted aerosol features measured by CATS during the nighttime, but for August and September of 2015 since CATS was not available in 2014.

As shown in Figure S3 and Table S1, the modeled ACA occurrence frequency is slightly higher than those retrieved from satellites in terms of the domain-averaged value. Due to the low sampling rate of CALIOP and CATS during the study period, the ACA occurrence frequencies as observed by these two satellites exhibit relatively noisy spatial patterns. Nevertheless, both observation and model roughly agree that there is a relatively high ACA occurrence frequency over the coastal region and a low ACA occurrence frequency over the remote region.

ACA-cloud mixing occurrence frequency

The ACA-cloud mixing occurrence frequency from CATS is derived following (*22*). We first examine ACA profiles observed by CATS. Out of all ACA profiles, we further examine whether aerosols appear in the pixels above the cloud-top, and calculate the mixing occurrence frequency. It should be noted that the vertical resolution of 60 m is the limitation of CATS satellite. When CATS detects that cloud tops and BB aerosol plume layers that are adjacent to each other, the possibility of aerosol mixing with cloud layers is high.

We calculated modeled ACA-cloud mixing occurrence frequency in a similar way. For model columns with ACA, we examine the model grids just above the cloud tops and check whether the extinction at wavelength 550 nm of model grids is larger than the threshold value (0.05 km^{-1}).

Upward shortwave flux at TOA ($SW_{TOA}\uparrow$)

In order to validate the modeled $SW_{TOA}\uparrow$, we use the CERES product “SYN1deg-3Hour” (https://ceres.larc.nasa.gov/science_information.php?page=CeresTempInterp), and average the values at 9, 12, 15 UTC over SEA.

Changes in cloud-top height due to BB aerosols

In the study by (*23*), they find that due to semi-direct effect-induced reduction in subsidence, the cloud-top height increases in the case with BB aerosols than the case without. Therefore, here we first examine the semi-direct effect-induced changes in subsidence.

We show subsidence profiles in both P-case and M-case (the difference between two cases represents the semi-direct effect) over the same region as in Figure 13a in (*23*), but for August-September instead of July-October. As stated in (*23*), the subsidence can be reduced by as much as one-third because of the semi-direct effect. As shown in Figure S13, the subsidence is also reduced in our simulation; however, the magnitude of peak reduction is about half of that from (*23*). The smaller reduction in subsidence can be due to 1) relatively smaller magnitude of semi-direct effect from this study; and 2) model differences between the two studies. For example, WRF-Chem is a nonhydrostatic model while CAM used in (*23*) is not. WRF-Chem simulations are conducted at a much higher horizontal resolution (3 km) compared to CAM simulations (~200 km).

Furthermore, as shown in both (*23*) and our study, BB aerosols are able to increase cloud-top height, while observational studies, like (*17*) and (*24*), show that cloud-top height decreases due to BB aerosols. Clearly, different approaches are adopted in modeling and observational studies.

One drawback in observational studies is that the role of meteorology can not be easily eliminated. For instance, (*17*) performed a statistical analysis and found that SST-binned CALIOP cloud-top heights are lower under denser BB aerosol plumes (aerosol index [AI] measured by Ozone Monitoring Instrument [OMI] > 2) in comparison with those in relatively clean regions (OMI AI<2). However, the BB aerosol loadings over the remote region are usually less dense than those near the coast, where the cloud-top heights are relatively lower, regardless of the presence of above-cloud BB aerosols. This implies that the co-variation of aerosol with meteorology in observational studies may have affected those results.

Here we follow the approach in (*24*), and only study the P-case and examine if we can reproduce the findings in (*24*).

Figure S14 shows the time series of above-cloud AOD and cloud-top height for entire September of 2014 as modeled by P-case. The values are averaged over a box around St. Helena Island (7.5° –17.5°S, 7.5°W–2.5°E) as in (*24*). In (*24*), AOD (fine mode)<0.1 and AOD (fine mode)>0.2 are defined as clean and polluted conditions, respectively. However, over all of September our model simulation predicts AOD higher than 0.1 over this region. Therefore, we use a slightly higher threshold to define the clean condition (AOD<0.15). In Figure S14, the two dashed lines represent two threshold values (0.15 and 0.2). We found that, in the P-case, the averaged cloud-top height of polluted condition is 183 m lower than that in clean conditions, in agreement with (*24*). It is likely that meteorology plays a role in determining the co-variance of cloud-top height and AOD. We speculate that it is due to some synoptic-scale dynamic systems propagating from east to west that control the aerosol transport process as well as the cloud properties over St. Helena Island. The underlying mechanisms are beyond the scope of this study.

Diurnal cycles of cloud-top heights

By examining the diurnal cycles of cloud-top heights modeled by three cases as shown in Figure S8, we find that, during the nighttime, about 50% of cloud-top height increase is due to enhanced entrainment, and the other half is due to reduced subsidence caused by the semi-direct effect (*23*). (This is a delayed impact on dynamics, as we find that the magnitude of reduced subsidence at cloud top during the nighttime is slightly smaller than the daily mean value shown in Figure S13.) During the daytime (i.e. from 9 UTC to 15 UTC), in addition to aforementioned two factors, the semi-direct effect of BB aerosols can strengthen the inversion and thereby reduce the cloud-top entrainment and cloud-top height (*17*, *25*). As a result, we find that the cloud-top height difference between P-case and M-case only accounts for about 20% of the cloud-top height difference between P-case and C-case. We note that, based on our estimation, the total effect of BB aerosols on cloud-top entrainment should still be positive during the daytime, because reduced subsidence alone cannot explain all the cloud-top height increase.

Stratocumulus-topped boundary layer (STBL) decoupling mechanism

As discussed in the main text, BB aerosols are able to increase cloud-top height partially because of higher entrainment rates; therefore, STBL also becomes deeper in both nighttime and daytime. In the daytime, solar heating at cloud top is able to counteract the cloud-top longwave cooling, which is the main source of the negative buoyancy eddies. Therefore the negative buoyancy eddies become weaker so that STBL is decoupled from the moisture supply from surface (the decoupling process) in the daytime. When STBL is deeper, the decoupling is more prone to happen because it becomes harder for the negative buoyancy eddies to mix through the sub-cloud layer.

Semi-direct effect of BB aerosols

The semi-direct effect predicted in this study is smaller but still comparable to that found in earlier studies [i.e., (*23*)].

In our study, sea surface temperature (SST) is fixed in all three cases. When we compared $\Delta_S\theta$ profiles (i.e., difference in potential temperature θ profiles between P-case and M-case) shown in Figure S15 against Figure 13a in (*23*) in the same region over the SEA, we found that although the heating rates by BB aerosol in higher altitudes (1.5 km to 3.5km) are similar, the WRF-Chem model predicts a small positive $\Delta_S\theta$ near the surface, because of heating by the BB aerosols entrained in the boundary layer. As a result, LTS (the difference in θ between 700 hPa and the surface, as defined in (*23*)) changes due to semi-direct effect (Δ_SLTS) predicted by WRF-Chem are smaller than that in (*23*) (0.21 K as shown in Figure S16 vs. 0.44-0.47 K). We note that (*23*) considered a longer period (July-October).

Whether or not surface cooling in WRF-Chem can cause a reduction in SST as significant as in the previous studies (e.g., (*23*)) remains unknown. In our study, BB aerosols in the P-case cause a domain-averaged daily mean surface cooling (i.e., surface SW flux reduction) over the ocean of -8.98 W m^{-2} compared to M-case. The magnitude appears to be comparable to the value (-10 W m^{-2}) reported in (*23*). However, over the same region as in our study, (*23*) in Figure 5j has a higher surface cooling than ours, around -20 W m^{-2}. If we included a slab ocean model in WRF similar to (*23*), the decrease of SST might be smaller than the value reported by (*23*) because of the lower surface cooling in our study.

Because of smaller Δ_SLTS, the CF changes due to the semi-direct effect of BB aerosols (Δ_SCF) are also smaller compared to the values reported in (*23*). In our study, we found that Δ_SCF is only significantly changed during the afternoon near the coastal region (+1%), while in (*23*) the domain-averaged daily Δ_SCF is +0.8% to +2%. The sum of the daily mean semi-direct and direct effects over the ocean is -1.04 W m^{-2} (+1.40 W m^{-2} over the coastal region and -2.81 W m^{-2} over the remote region) in our study. The sum of the daily mean semi-direct and direct effects estimated by (*23*) is around -1.7 to -0.8 W m^{-2}. Again, (*23*) considered a longer period (July-October) and larger region.

Since this study focuses on the microphysical effects of BB aerosols the quantitative difference in the semi-direct effect between our and other studies will not change the conclusions of our study.

Contributions of N_d, CF and LWP to changes in upward shortwave fluxes at TOA ($SW_{TOA}\uparrow$)

To further examine the contributions from CF, LWP and N_d to upward shortwave flux at TOA ($SW_{TOA}\uparrow$), we follow the same approach as in (*26*). For instance, the change in $SW_{TOA}\uparrow$ due to changes in CF is calculated by

$$\Delta SW_{CF} = SW(CF_M, LWP_C, Nd_C) - SW(CF_C, LWP_C, Nd_C),$$

where subscripts M and C represent cloud properties modeled by M-case and C-case, respectively. SW is a parameterized $SW_{TOA}\uparrow$, which is a function of CF, LWP, and N_d, and is calculated using equations C1~C5 in (*26*). The magnitude of parameterized SW(CF_C, LWP_C, Nd_C) averaged over 9UTC, 12UTC, and 15UTC is 8.69% higher than modeled $SW_{TOA}\uparrow$ in C-case. It is worthy to mention that, according to (*27*), the uncertainties in CERES fluxes are less than 5% for SW for overcast, moderately thick or thick low clouds over ocean.

The contribution of changes in CF to the total microphysical effect is calculated by

$$P_{CF} = \frac{\Delta SW_{CF}}{\Delta SW_{CF} + \Delta SW_{LWP} + \Delta SW_{Nd}}$$

In (*26*), cloud properties modeled at different time steps are first weighted by downward SW flux at TOA, and then used in the calculation. In our study, we first calculate ΔSW_{CF}, ΔSW_{LWP}, ΔSW_{Nd} at 9UTC, 12UTC, and 15UTC, and scale these three variables so that the sum of three variables equals the modeled changes in $SW_{TOA}\uparrow$ between the M-case and C-case at 9, 12, and 15 UTC, respectively. We then average each variable at three times, and finally calculate the contribution. The results show that CF, LWP and N_d contribute to the total microphysical effect by 1.05%, 21.09%, and 77.86%, respectively, averaged over the three times. Therefore, the Twomey effect contributes the most to the microphysical effect. The lower CF effect is because of the cancellation of increased CF in the morning and decreased CF in the afternoon (Figure 2D) due to the microphysical effect.

Precipitation efficiency

In (*28*), the cloud-base rain rate of stratocumulus is parameterized as a function of LWP and N_d. Using domain-averaged LWP and N_d values at 12UTC in P-case and C-case, we find that parameterized cloud-base rain rates in two cases equal to 0.0101 mm h^{-1} and 0.0276 mm h^{-1}, respectively. In comparison, domain-averaged surface rain rates at 12UTC as modeled by P-case and C-case are 0.015 mm h^{-1} and 0.019 mm h^{-1}, respectively (cloud-base rain rate is not outputted in the model). The difference between parameterized and modeled rain rates is within the error (60%) associated with the parameterized cloud-base rain rate in (*28*). The fact that the rain rate in the P-case is smaller than the C-case also proves that precipitation is suppressed because of BB aerosols.

Spatial pattern of LWP change

By examining the ΔLWP spatial distribution at 15 UTC in Figure S5, we find that the P-case predicts smaller LWP compared to the C-case over a small area in the remote region (2°S to

10°S, 10°W to 17°W), where the precipitation rate at 15 UTC predicted by the P-case is below 0.1 mm day^{-1}. This result is in agreement with (*9*), who found that stratocumulus clouds become thinner with increasing N_d if the precipitation rate is small (<0.1 mm day^{-1}). Higher N_d can enhance cloud-top entrainment due to faster evaporation of smaller cloud droplets. The response of cloud water to increasing N_d depends on the competition between moistening from decreased precipitation and drying from increased entrainment. It is only when sufficient precipitation reaches the surface and moistens the boundary layer that LWP increases with increases in N_d. It is worth noting that the area with decreasing LWP is where stratocumulus cloud decks are transitioning into trade-wind cumulus clouds.

Validation of WRF-Chem model against WRF-LES model

The impacts of BB aerosols on the cloud diurnal cycle modeled in WRF-Chem are further validated against WRF-LES results, since the performance of WRF-Chem can be limited by its relatively coarse resolution (*29*). To facilitate the comparison, we ran four one-way nesting simulations (denoted as d01 to d04) for the same two-day period over different regions of the SEA, so that our WRF-LES results represent the evolution of stratocumulus clouds under the influence of BB aerosols over different regions. The results from WRF-LES simulations demonstrate that, in agreement with previous studies (*9*), the effects of BB aerosols on cloud properties depend on whether precipitation reaches the surface. Figure S6 shows the diurnal cycles of ΔLWP and ΔCF from WRF-LES simulations, for periods when domain-averaged precipitation rates in the P-case exceed 0.1 mm day^{-1}. The result shows that the impact of BB aerosols on cloud properties differs depending on the domain. For the domains that are closer to the coast (d01 and d02), ΔCF are very small, around 0.2%, from mid-night to early morning, because the clouds are nearly overcast over those domains (Figure S6 (C)). The significant increases in LWP during the same period are in agreement with the WRF-Chem simulation over the coastal region. For the domain d04, which is relatively far from the coast, ΔCF experiences more dramatic changes. As shown in Figures S6 (D) and (E), ΔCF for domain d04 changes from +7% to -6% in 5 hours, demonstrating the effect of BB aerosols on entrainment and subsequently cloud breakup. Interestingly, the average ΔLWP and ΔCF over the four domains agrees reasonably well with WRF-Chem simulation over the coastal region, except during the evening (21 UTC) when ΔLWP is lower.

For the entire simulation period as shown in Figure S7, the average ΔLWP of the four model domains still agrees reasonably well with the WRF-Chem results. From 18 UTC to 21 UTC, WRF-LES disagrees with WRF-Chem in terms of simulating ΔCF: the former yields negative average values (~ -4%) while the latter predicts small positive values (~1%). This WRF-LES result indicates that the recovery of the cloud deck during early evening (i.e. negative ΔCF during 18 UTC~21 UTC) is delayed when the precipitation rate is extremely small (i.e. < 0.1 mm day^{-1}). The discrepancy between WRF-Chem and WRF-LES for ΔCF does not weaken our findings with WRF-Chem, since precipitation rates modeled by WRF-Chem usually exceed 0.1 mm day^{-1} during early evening (18 UTC~21 UTC).

References in SI Appendix:

1. Grell GA, et al. (2005) Fully coupled "online" chemistry within the WRF model. *Atmos Environ* 39(37):6957–6975.
2. Ichoku C, Ellison L (2014) Global top-down smoke-aerosol emissions estimation using satellite fire radiative power measurements. *Atmos Chem Phys* 14(13):6643–6667.
3. Freitas SR, et al. (2007) Including the sub-grid scale plume rise of vegetation fires in low resolution atmospheric transport models. *Atmos Chem Phys* 7(13):3385–3398.
4. Wiedinmyer C, et al. (2011) The Fire INventory from NCAR (FINN): a high resolution global model to estimate the emissions from open burning. *Geosci Model Dev* 4(3):625–641.
5. Lu Z, Sokolik IN (2013) The effect of smoke emission amount on changes in cloud properties and precipitation: A case study of Canadian boreal wildfires of 2007. *J Geophys Res: Atmos* 118(20):11777–11793.
6. Yang Q, et al. (2011) Assessing regional scale predictions of aerosols, marine stratocumulus, and their interactions during VOCALS-REx using WRF-Chem. *Atmos Chem Phys* 11(23):11951–11975.
7. Abdul-Razzak H, Ghan SJ (2000) A parameterization of aerosol activation: 2. Multiple aerosol types. *J Geophy Res: Atmos* 105(D5):6837–6844.
8. Yamaguchi T, Feingold G, Kazil J, McComiskey A (2015) Stratocumulus to cumulus transition in the presence of elevated smoke layers. *Geophy Res Lett* 42(23):10478–10485.
9. Ackerman AS, Kirkpatrick MP, Stevens DE, Toon OB (2004) The impact of humidity above stratiform clouds on indirect aerosol climate forcing. *Nature* 432(7020):1014-1017.
10. Wang H, Feingold G (2009) Modeling mesoscale cellular structures and drizzle in marine stratocumulus. Part I: Impact of drizzle on the formation and evolution of open cells. *J Atmos Sci* 66(11):3237–3256.
11. Feingold G, et al. (2010) Precipitation-generated oscillations in open cellular cloud fields. *Nature* 466(7308):849-852.
12. Wang H, Feingold G, Wood R, Kazil J (2010) Modelling microphysical and meteorological controls on precipitation and cloud cellular structures in Southeast Pacific stratocumulus. *Atmos Chem Phys* 10(13):6347–6362.
13. Talbot C, Bou-Zeid E, Smith J (2012) Nested mesoscale large-eddy simulations with WRF: performance in real test cases. *J Hydrometeor* 13(5):1421-1441.
14. Smagorinsky J (1963) General circulation experiments with the primitive equations: I. The basic experiment. *Mon Wea Rev* 91(3):99-164.
15. Meyer K, Platnick S, Zhang Z (2015) Simultaneously inferring above-cloud absorbing aerosol optical thickness and underlying liquid phase cloud optical and microphysical properties using MODIS. *J Geophys Res: Atmos* 120(11):5524-5547.
16. George RC, Wood R (2010) Subseasonal variability of low cloud radiative properties over the southeast Pacific Ocean. *Atmos Chem Phys* 10(8):4047–4063.
17. Wilcox E (2012) Direct and semi-direct radiative forcing of smoke aerosols over clouds. *Atmos Chem Phys* 12(1):139-149.

18. Winker, DM, et al. (2013) The global 3-D distribution of tropospheric aerosols as characterized by CALIOP. *Atmos Chem Phys* 13(6):3345-3361.
19. Vaughan MA, et al. (2009) Fully automated detection of cloud and aerosol layers in the CALIPSO lidar measurements. *J Atmos Oceanic Technol* 26(10):2034–2050.
20. Zhang Z, et al. (2016) Shortwave direct radiative effects of above-cloud aerosols over global oceans derived from 8 years of CALIOP and MODIS observations. *Atmos Chem Phys* 16(5):2877-2900.
21. Meyer K, Platnick S, Oreopoulos L, Lee D (2013) Estimating the direct radiative effect of absorbing aerosols overlying marine boundary layer clouds in the southeast Atlantic using MODIS and CALIOP. *J Geophy Res: Atmos* 118(10):4801-4815.
22. Rajapakshe C, et al. (2007) Seasonally transported aerosol layers over southeast Atlantic are closer to underlying clouds than previously reported. *Geophys Res Lett* 44:5818-5825.
23. Sakaeda N, Wood R, Rasch PJ (2011) Direct and semidirect aerosol effects of southern African biomass burning aerosol. *J Geophy Res: Atmos* 116(D12):D12205.
24. Adebiyi AA, Zuidema P, Abel SJ (2015) The convolution of dynamics and moisture with the presence of shortwave absorbing aerosols over the southeast Atlantic. *J Clim* 28(5):1997–2024.
25. Johnson B, Shine K, Forster P (2004) The semi-direct aerosol effect: Impact of absorbing aerosols on marine stratocumulus. *Q J R Meteorol Soc* 130(599):1407-1422.
26. Grosvenor DP, Field PR, Hill AA, Shipway BJ (2017) The relative importance of macrophysical and cloud albedo changes for aerosol-induced radiative effects in closed-cell stratocumulus: insight from the modelling of a case study. *Atmos Chem Phys* 17: 5155-5183.
27. Loeb NG, Kato S, Loukachine K, Manalo-Smith N, Doelling DR (2007) Angular distribution models for top-of-atmosphere radiative flux estimation from the clouds and the earth's radiant energy system instrument on the Terra satellite. part II: validation. *J Atmos Ocean Tech* 24: 564–584.
28. Comstock KK, Wood R, Yuter SE, Bretherton CS (2004) Reflectivity and rain rate in and below drizzling stratocumulus. *Q J R Meteorol Soc* 130: 2891-2918.
29. Martini MN, Gustafson WI, Yang Q, Xiao H (2014) Impact of resolution on simulation of closed mesoscale cellular convection identified by dynamically guided watershed segmentation. *J Geophys Res: Atmos* 119(22): 12674–12688.

Table S1. Modeled cloud and aerosol properties in comparison with satellite retrievals averaged over the SEA and study period. Observed CF, LWP, and N_d are obtained from MODIS/Terra in the morning (AM) and MODIS/Aqua in the afternoon (PM). Observed CF ranges are obtained from the SEVIRI satellite at 10:30 LST and 13:30 LST. Uncertainties associated with LWP and ranges of N_d are discussed in the SI. Observed ACA frequencies are obtained from [a]CALIOP nighttime observation, [b]CATS nighttime observation (for Aug.-Sept. of 2015).

	CF/AM (%)	CF/PM (%)	LWP/AM (g/m^2)	LWP/PM (g/m^2)	N_d/AM (# cm^{-3})	N_d/PM (# cm^{-3})	ACA freq. (%)
Satellite observations	65.9 (65.3-75.0)	57.8 (56.4-70.6)	86.2±10.2	70.1±8.0	92.5 (63.9 - 128.6)	85.3 (59.3-132.9)	[a]60.1, [b]63.0
P-case	67.0	57.5	83.3	70.8	90.6	91.5	66.5
C-case	66.5	59.0	76.1	65.2	44.6	47.1	
M-case	66.8	57.2	82.7	69.4	90.9	92.0	

Figures in SI Appendix:

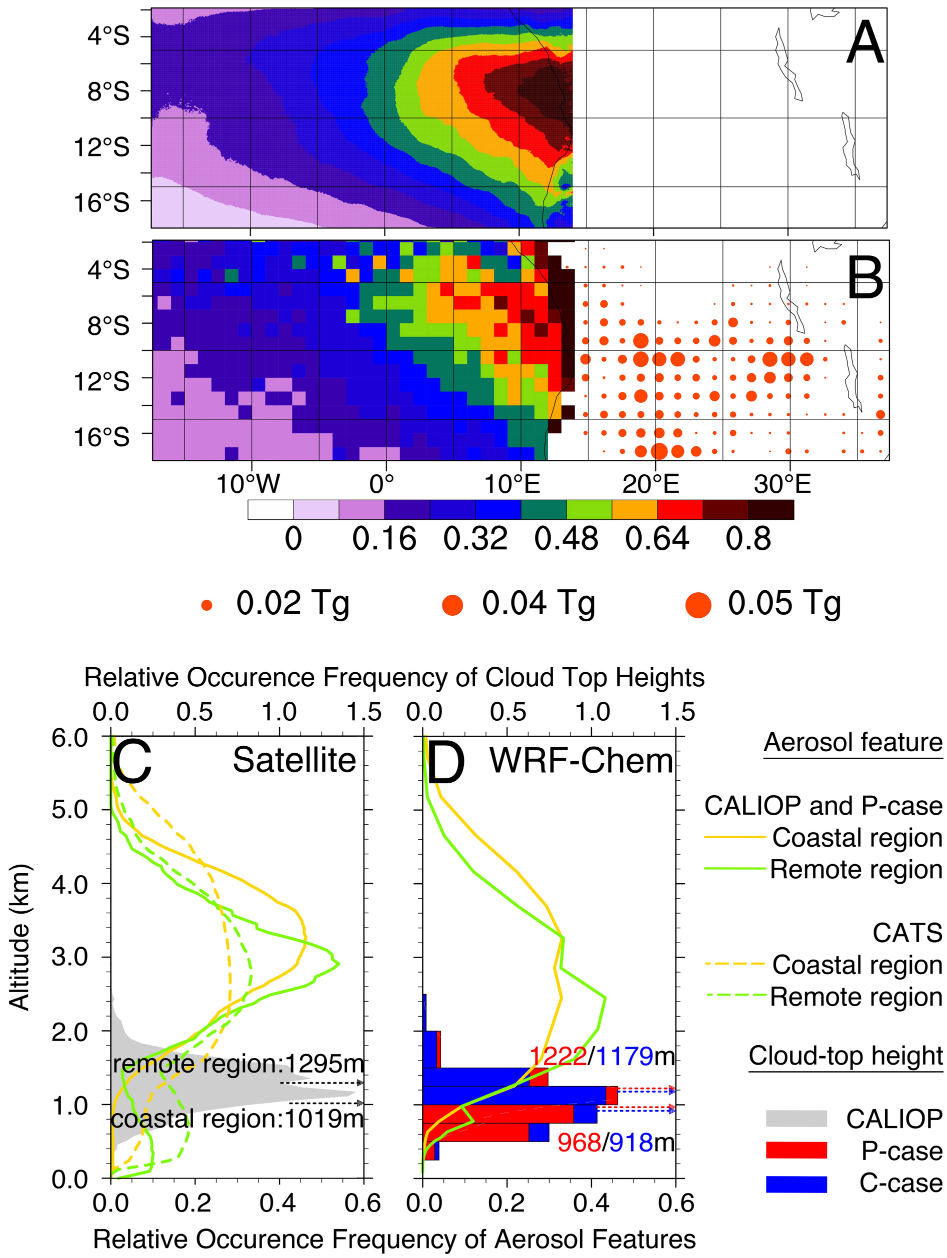

Figure S1. Simulation period mean above-cloud AOD fields over SEA as (A) modeled by P-case and (B) observed by MODIS/Aqua for the local afternoon. The dots represent 2-month BB aerosol emissions over an area of 150 km by 150 km. Simulation period mean vertical distributions of BB aerosols for nighttime cloudy-sky profiles over SEA as (C) observed by CALIOP and CATS and (D) modeled by P-case. The yellow and green curves represent the vertical distribution of BB aerosols averaged over the two-month study period and over the coastal and remote regions, respectively (for observed and modeled vertical distributions of aerosol features, the remote region is defined as 5°W to 17°W, 2°S to 17°S to highlight the differences in profiles). Also shown in (C and D) is relative occurrence frequency of cloud top height as observed by CALIOP (grey shaded area) and modeled by the P-case (red bars) and C-case (blue bars) in the daytime during the simulation period. The arrows label observed and modeled mean cloud top heights over the coastal and remote regions.

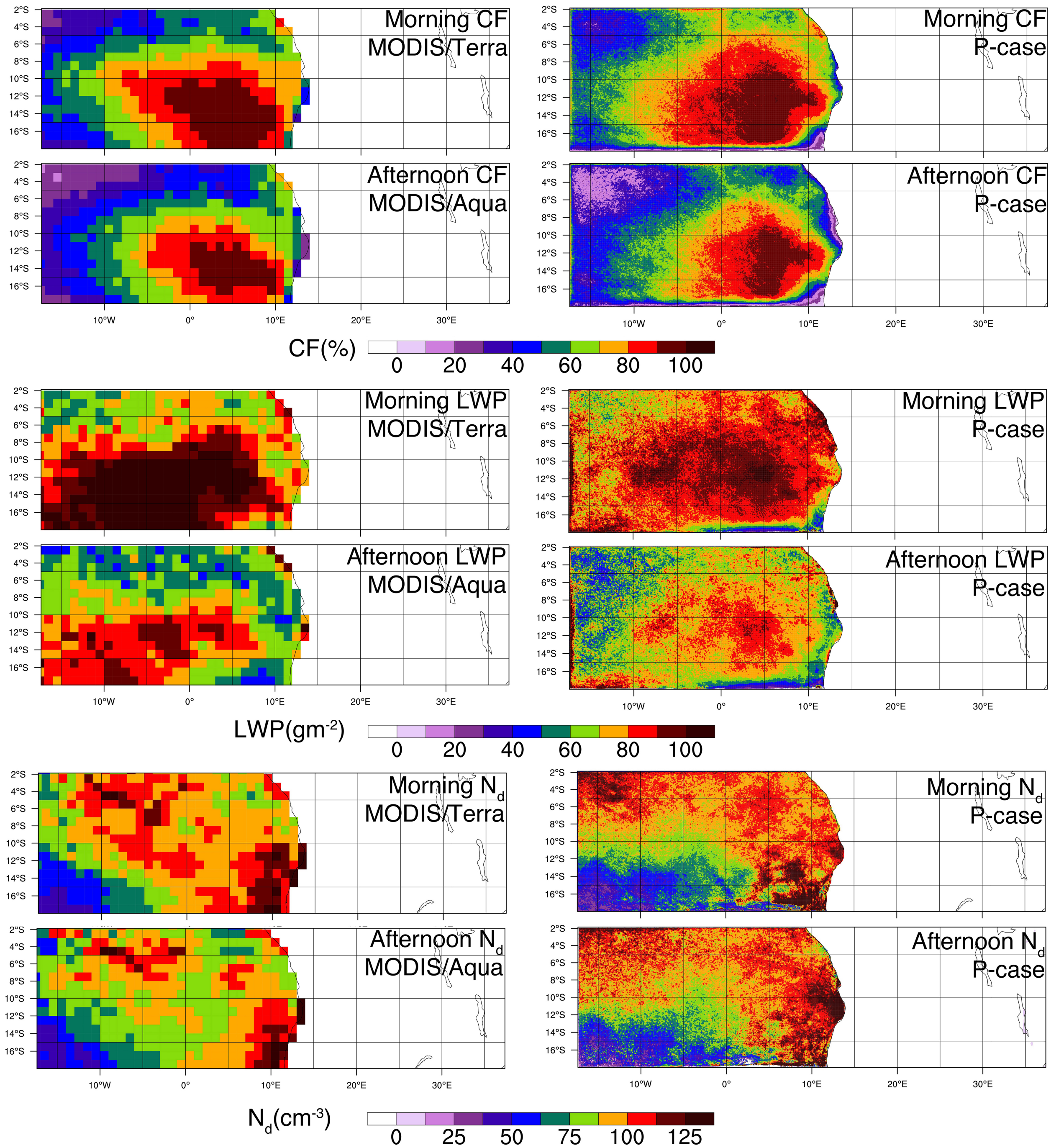

Figure S2. Left column: MODIS observations of CF (unit: %), LWP (unit: gm^{-2}), and cloud-top N_d (unit: cm^{-3}) during morning (Terra/MODIS) and afternoon (Aqua/MODIS) averaged over the study period; Right column: modeled CF, LWP, and N_d during morning and afternoon averaged over the study period.

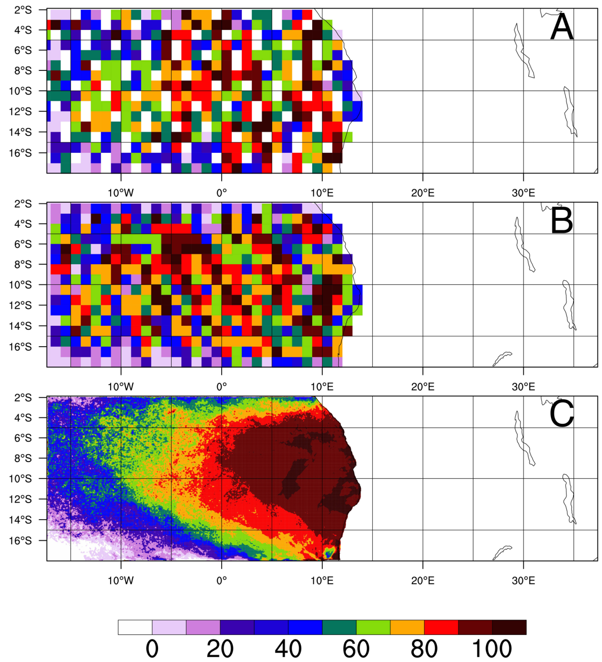

Figure S3. Nighttime ACA occurrence frequency as A) observed by CALIOP, B) observed by CATS, and C) modeled by P-case during the nighttime for the study period (unit: %).

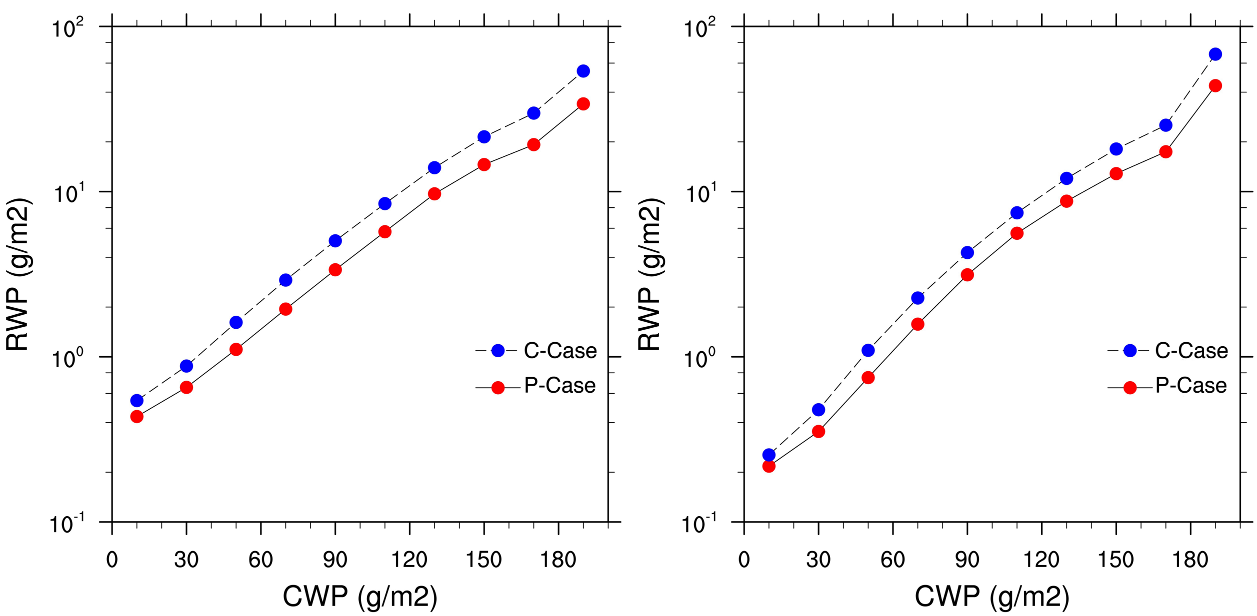

Figure S4. Distribution of rain water path (RWP) binned by cloud water path (CWP). RWP and CWP at 6 UTC (left) and 12 UTC (right) are modeled by P-case and C-case over SE Atlantic during the study period. It is clear that, for a fixed CWP, P-case predicts less RWP, indicating that rain formation is suppressed by BB aerosols.

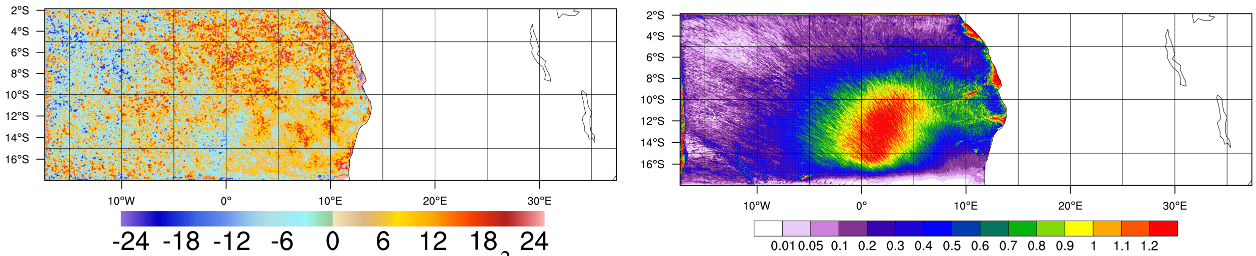

Figure S5. LWP difference (unit: g m^{-2}) between P-case and C-case at 15 UTC averaged over the study period (left), and precipitation rate of P-case (unit: mm day^{-1}) (right) at 15 UTC averaged over study period.

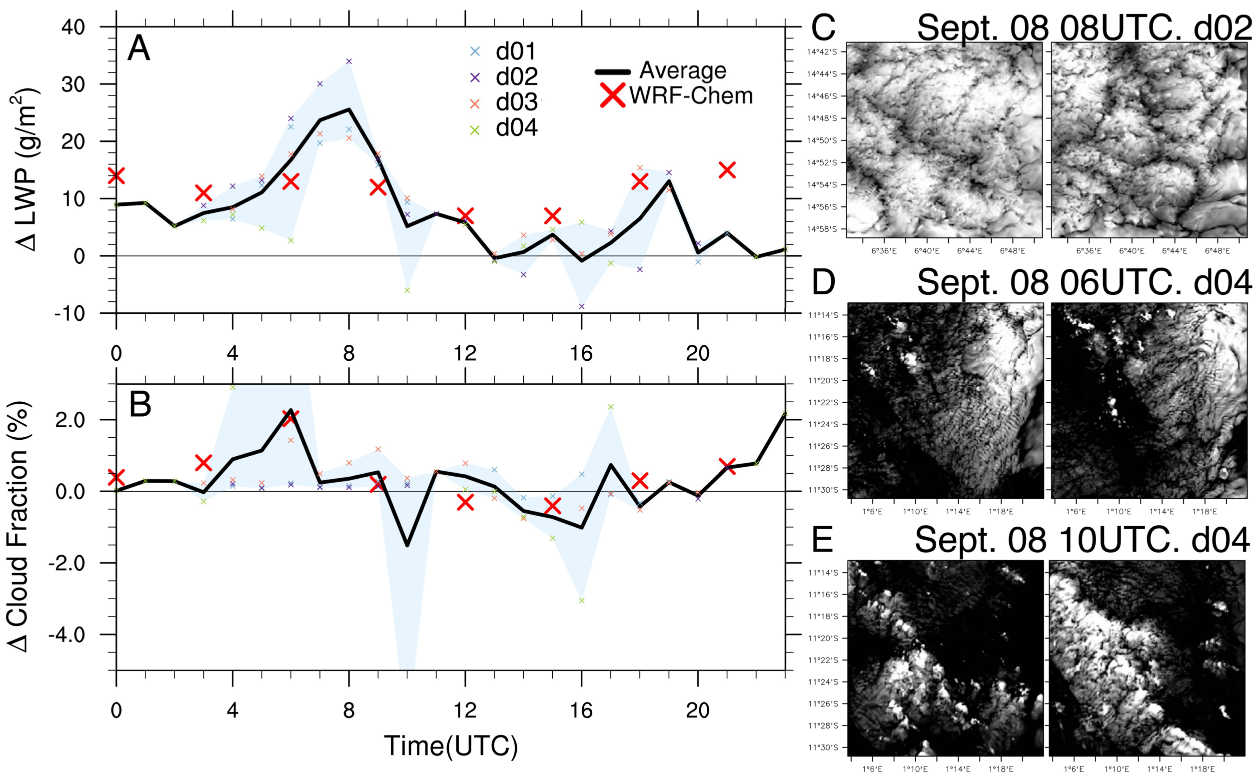

Figure S6. Differences in A) LWP and B) CF between P-case and C-case as modeled by four one-way nesting WRF-LES simulations near the coastal region. Only the time periods when domain-averaged precipitation rates exceed 0.1 mm d^{-1} are considered. The black line represents the average value of the four cases, while light-blue shaded area indicates the range of the four cases. Red crosses represent ΔLWP and ΔCF modeled by WRF-Chem simulation over the coastal region. Shown in C), D), and E) are three instantaneous LWP fields modeled by P-case (left column) and C-case (right column) using WRF-LES. The gray scale ranges from 0 to 240 g m^{-2}.

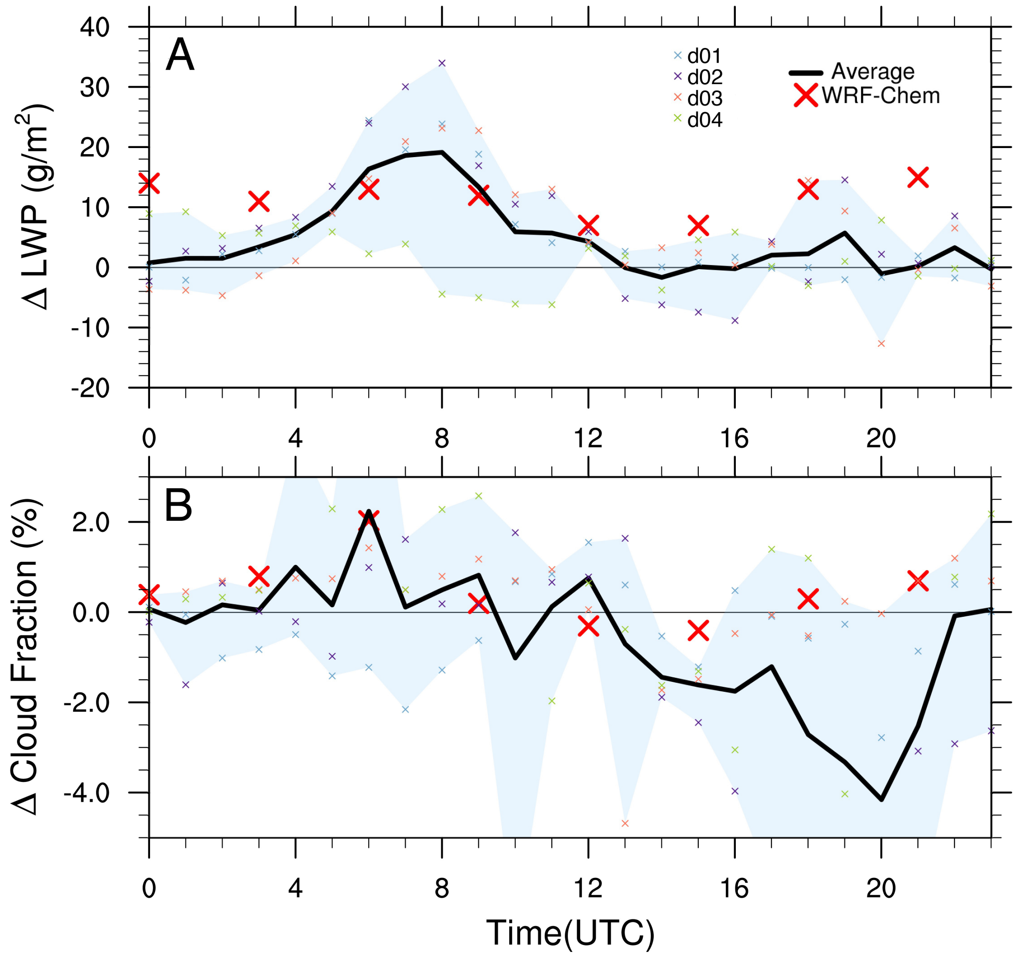

Figure S7. Similar as Figure S6 (A and B), but for all period (without filtering by precipitation rate).

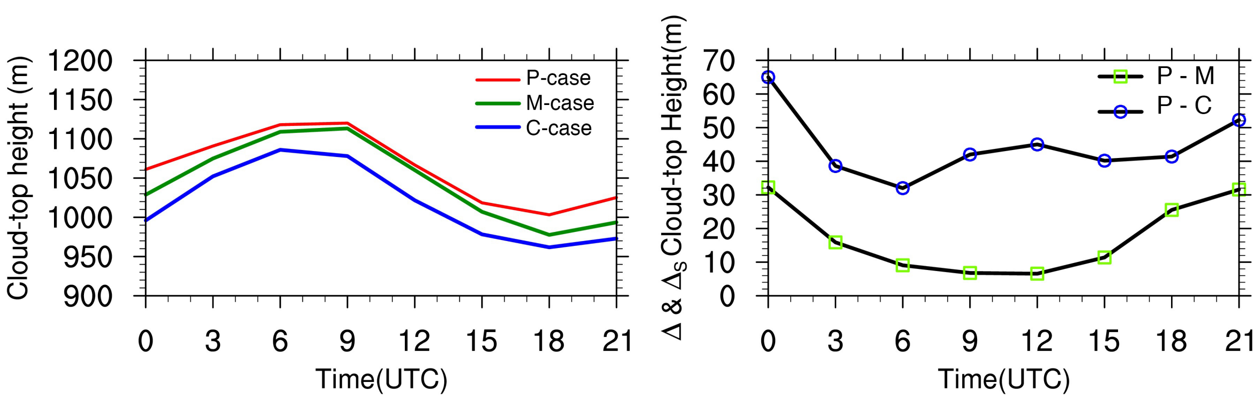

Figure S8. Left: diurnal cycles of cloud-top heights modeled by P-case (red line), C-case (blue line), and M-case (green line) averaged over SEA and study period. Right: diurnal cycles of cloud-top height differences between P- and M-cases and P- and C-cases.

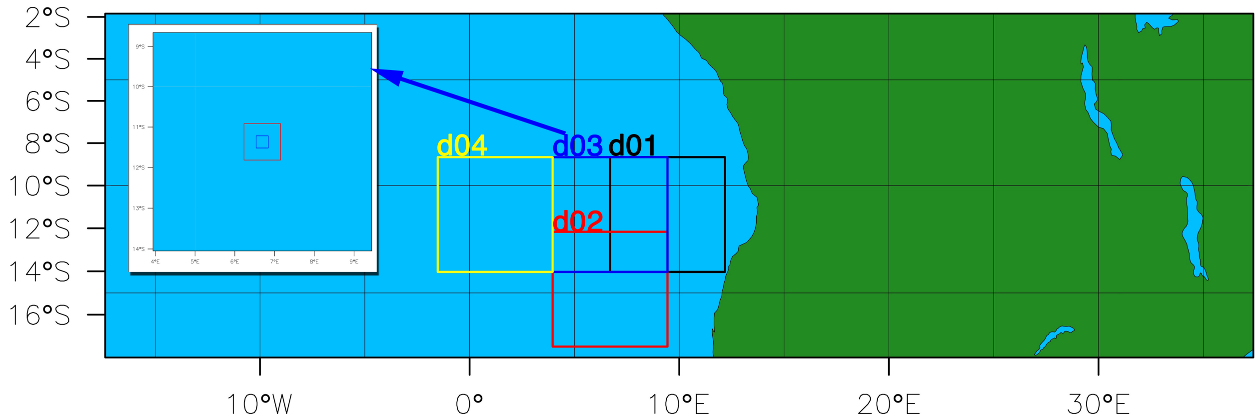

Figure S9. WRF-Chem modeling domain, with four sub-domains labeled by squares. Each one-way nesting simulation is run with two additional levels of nesting.

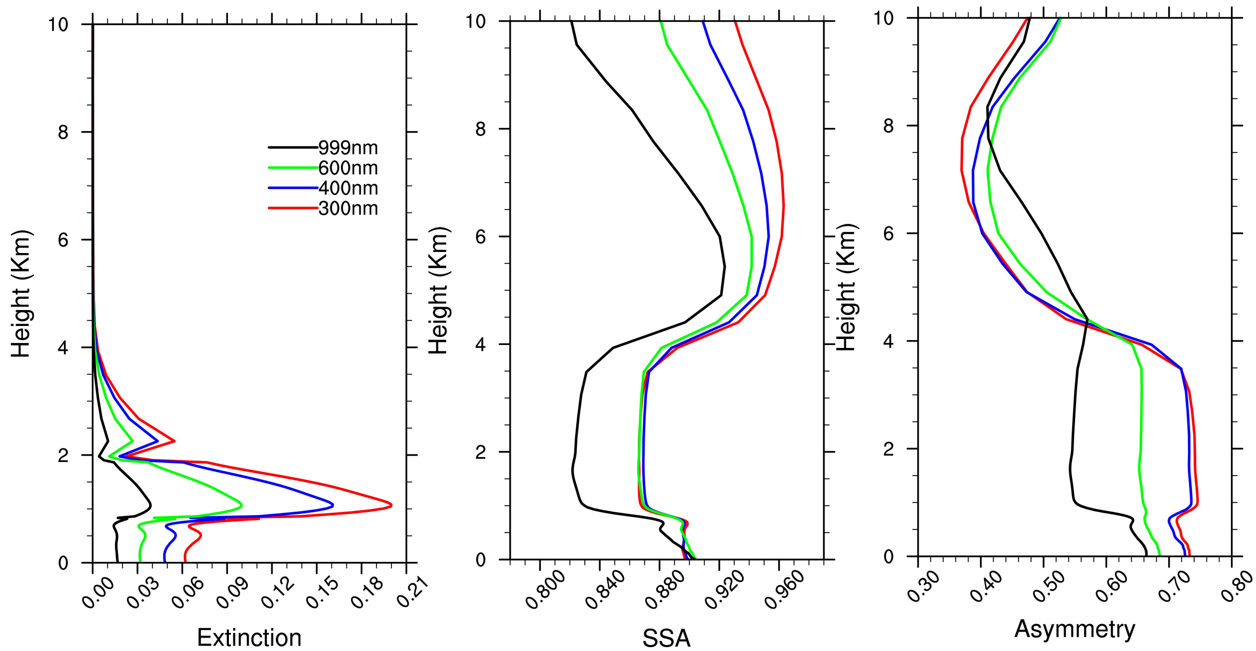

Figure S10. From left to right: profiles of extinction (unit: km^{-1}), single scattering albedos, and asymmetry factors at wavelengths of 300, 400, 600, and 999 nm, embedded in WRF-LES simulations.

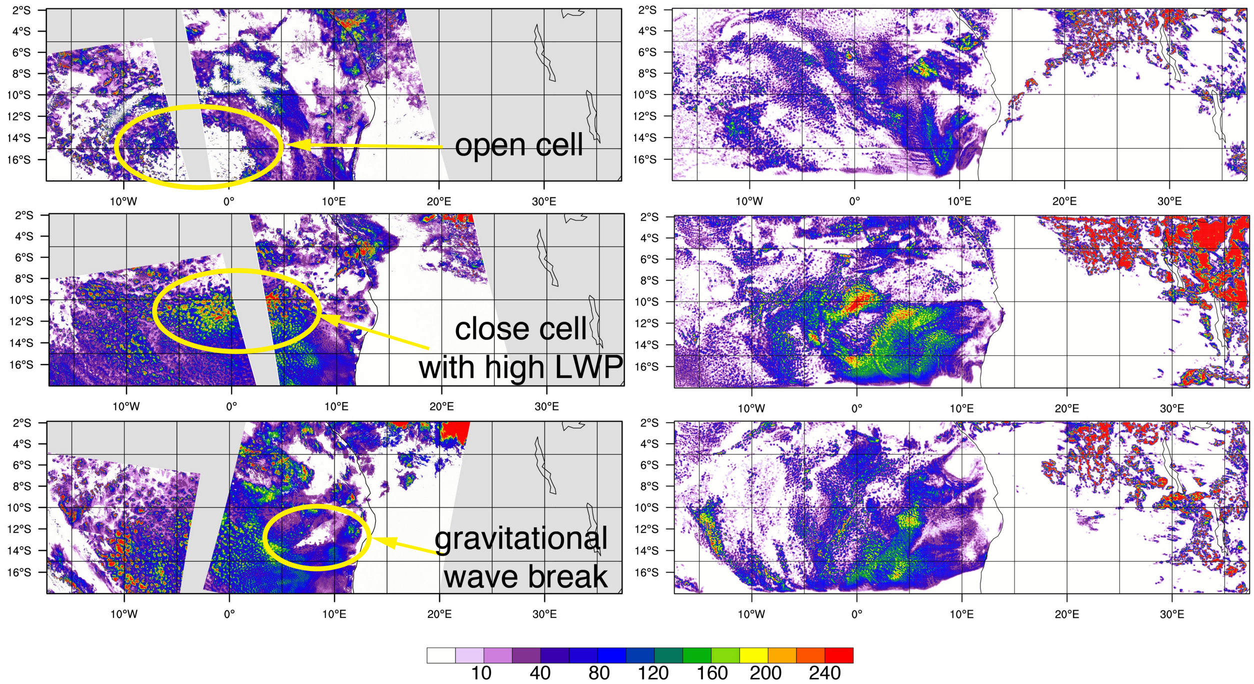

Figure S11. From top to bottom, MODIS level-2 cloud water path product (left column, from Aqua or Terra satellites) in comparison with modeled LWP (unit: kg m^{-2}) at 12 UTC (right column) on September 2, September 5, and September 7, respectively (from top to bottom).

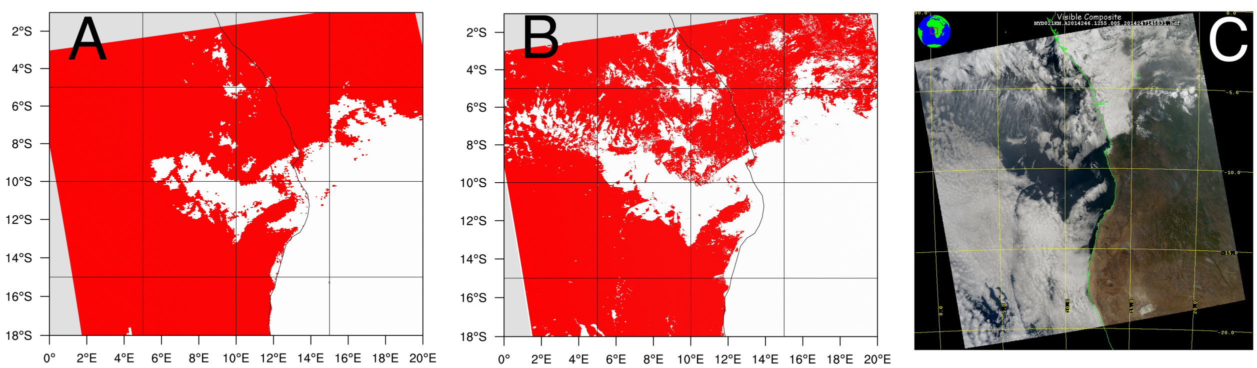

Figure S12. (A) "Cloud Fraction" product non-zero pixels, (B) "Cloud Water Path" product non-zero pixels, and (C) "True color image" product as observed by Aqua/MODIS on September 3, 2014. Pixels with non-zero "Cloud Fraction" or "Cloud Water path" are labeled by red color. "True color image" is downloaded from https://ladsweb.nascom.nasa.gov

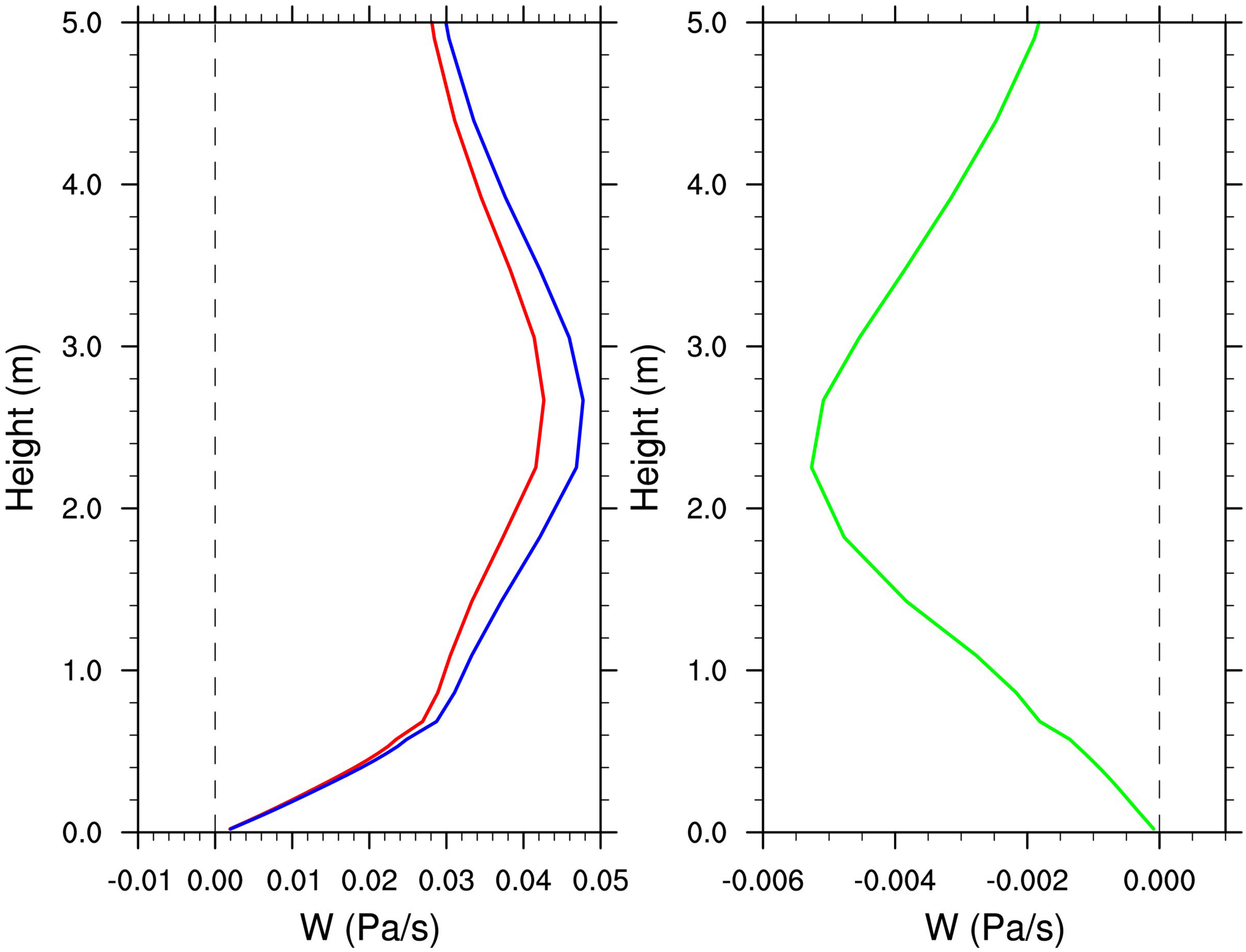

Figure S13. Left: Profiles of vertical velocities predicted in P-case (red solid line) and M-case (blue solid line); right: the difference in vertical velocities between two cases.

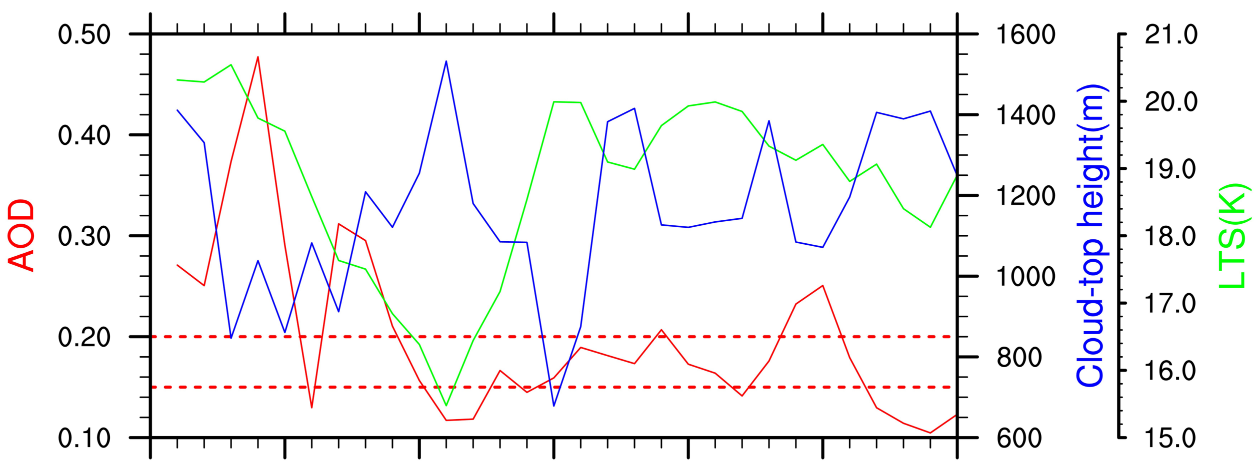

Figure S14. Time series of "P" case modeled above-cloud AOD (in red), cloud-top height (in blue), and LTS (between 800 hPa and surface) (in green) for September averaged over a box around St. Helena Island as in (*24*). The red dashed lines show the thresholds for clean-moderate-polluted conditions, defined similarly as in (*35*).

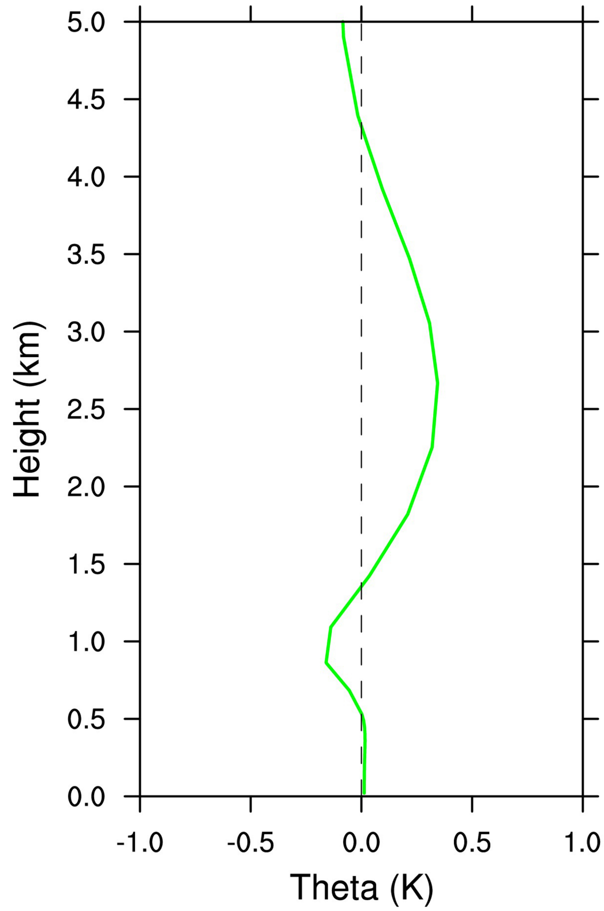

Figure S15. Difference in potential temperature profiles between P-case and M-case as modeled by WRF-Chem in our study. The study area in (*18*) is also adopted in this study.

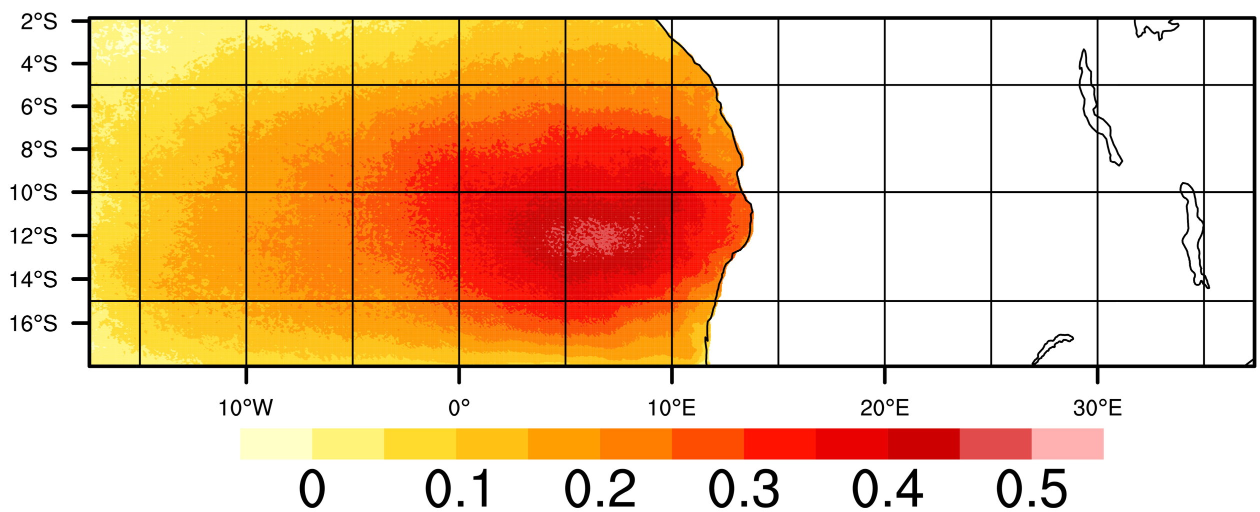

Figure S16. Difference in daily mean LTS fields between P-case and M-case during the study period.